SEMARAK ILMU PUBLISHING

CFD Letters

Journal homepage:
https://semarakilmu.com.my/journals/index.php/CFD_Letters/index
ISSN: 2180-1363

The Dimple Effect on Flettner Rotors for the Wind Power Drive System of a Sailing Merchant Ship

Aries Sulisetyono[1,*], Aditya Bagaskara[1]

[1] Department of Naval Architecture, Faculty of Marine Technology, Institut Teknologi Sepuluh Nopember, Kampus ITS Sukolilo 60111, Surabaya, Indonesia

ARTICLE INFO

Article history:
Received 15 May 2023
Received in revised form 17 June 2023
Accepted 15 July 2023
Available online 10 December 2023

Keywords:
computational fluid dynamic; flettner rotor; wind power drive system; dimpled surface

ABSTRACT

Wind-powered ship propulsion is investigated in relation to reducing ship exhaust emissions, such as the application of Flettner rotor systems. How to increase rotor thrust's contribution to ship speed is an intriguing research question. This paper investigates the influence of dimples on the surface of a Flettner rotor on its ability to generate thrust for a ship. The CFD code, which includes the Reynolds average Navier-Stokes equation and the k-ω model for turbulent flow, is utilized to analyse three rotor designs: one with a smooth surface and two with dimple surfaces of varying diameters. Lift and drag are computed by taking into account varying spin ratios and the incoming wind angle. The CFD results are validated by comparing them to experimental data gathered in a wind tunnel and determining that their error is less than 5%. The addition of dimpled surfaces to the rotor increases lift by 69.6% and decreases drag by 14.8% due to the smooth surface. For the case study, the two rotors are mounted on the sailing ship 900 DWT and can generate the most thrust to give the ship a speed of 8.5 knots with a spin ratio of 4 and apparent wind angles of 90^o or 270^o relative to its speed.

1. Introduction

Modern ship propulsion systems use a variety of wind-powered technologies, including soft sails, rigid sails, sky sails, Flettner rotor sails, and many others [1-3]. In comparison to a conventional sail device, a Flettner rotor offers a number of benefits, the most notable of which are (i) a smaller footprint on the deck of the vessel, (ii) a reduced number of crew members required, and (iii) increased propulsion [4]. According to the results of the experiments, a Flettner rotor sail has better performance in terms of generating thrust than soft sails [4]. In theory, a Flettner rotor makes use of the Magnus effect phenomenon, which Anton Flettner discovered [5] and applied to the shipping industry on the Schooner Buckau ship [6]. The E-Ship-1 ship deployed a hybrid propulsion system that consisted of the Flettner rotors and the diesel engines during a trial cruise of 170,000 nautical miles, which resulted in about a 25% reduction in fuel consumption [2].

* *Corresponding author.*
E-mail address: sulisea@na.its.ac.id (Aries Sulisetyono)

https://doi.org/10.37934/cfdl.16.2.7690

Numerous researchers have previously studied the Flettner rotor design using both numerical and experimental methods [7, 8]. The majority of research, however, holds that the rotor's design—including its diameter, height, rotational speed, and rotor surface—as well as external elements like wind speed and density, have an impact on the thrust of a rotor. The design of a rotor can be boiled down to three primary parameters: the aspect ratio (AR), which is the ratio between the height and the diameter of the rotor; and the spin ratio (SR), which is the ratio between the speed of the rotor's rotation and the speed of the incoming wind [7]. The results of the experiments confirmed the results of the STAR-CCM+ software analysis, which showed that the aerodynamic efficiency of the Flettner rotor improved most when SR was set to 3 and AR was set to 8 [7]. A novel type of rotor that can be mounted on a ship's superstructure has been conceived, which is constructed in the shape of a cylinder to reduce wind friction [9].

The theory suggests that it may be possible to improve the performance of the Flettner rotor in terms of its ability to generate lift and drag by increasing the surface roughness [10]. It is claimed that the change from a laminar to a turbulent boundary layer at a given Reynolds number (Re) is the cause of the reduction in drag due to surface roughness. The principle is to manage the separation of flow and wake on the cylinder surface. Previous studies have taken into consideration a wide variety of surface roughness patterns, some of which include surface trip wire, roughness strips, dimples, grooves, helical stripes, screened surfaces, and so on [10]. Over the Reynolds number range of 2 x 10^4 to 3 x 10^5, the dimpled surface could have a big effect on reducing drag in cylinders [11], and over the range of Re = 3.14 x 10^4 to 2.88 x 10^4, it could achieve a drag coefficient that is about 0.65 times that of a smooth surface in the ratio of the dimple depth to the diameter of 1.98 x 10^{-2} [12]. Experiments were also conducted in open water channels with Reynolds numbers ranging from 7.43 x 10^3 to 1.798 x 10^4, resulting in the conclusion that a dimpled surface with a ratio of the dimple depth to the diameter of 0.05 could produce a drag coefficient that was nearly 90% that of a smooth cylinder [10]. Yahaya *et al.,* [13] proposed a grooved cylinder to relocate a separation point on the cylinder's surface, thereby decreasing the drag coefficient. The flow past a circular cylinder with smooth, half-and-full rectangular, grooved surfaces was studied in a low-speed, open-ended wind tunnel. At Re = 1 x 10^5, the complete grooves confronting the flow produced up to 55% less resistance than a smooth cylinder. Research on the aerodynamic properties of a golf ball with a smooth surface and a dimpled surface [14] in terms of the production of lift and drag coefficients under rotating and non-rotating ball conditions served as the inspiration for the Flettner rotor's dimpled surfaces. The simulation of golf balls with diameters of 42.6 mm and 100 mm was conducted using a three-dimensional numerical model (CFD) approach and wind tunnel model testing. The results of this simulation indicate that an increase in spin rate causes the lift coefficient of golf balls with dimpled surfaces to increase considerably compared to those with smooth surfaces. This phenomenon motivates researchers to create dimples on the surface of a rotor in the belief that it will increase the rotor's thrust force.

The 900-DWT sailing merchant vessel ‘Maruta Jaya’ served as the subject of the study case to find out the possible benefits of installing the Flettner rotors design in terms of generating thrust against the average wind speed in Indonesia. This vessel has been seen sailing across Indonesian waters using a combination of DC engines and soft sails as its propulsion method. However, the contribution of the soft sails to providing thrust to the vessel is still relatively low, especially during low wind gusts. The rigid sails have also been proposed to replace soft sails on this ship, where the study concluded that there was an increase in thrust under certain conditions of wind direction and speed [3]. This paper proposes a suitable dimpled rotor design as an alternative to the soft sail that has been used on the ‘Maruta Jaya’ sailing vessel. The previously conducted and published study is expanded upon in this paper by carefully examining the effect that the essential parameters SR and wind incidence

angle have on the performance of the dimpled Flettner rotor in generating driving power. All of the analyses are performed with a program for computational fluid dynamics technique that is available for commercial use, and the findings of the rotor model test in the wind tunnel that was published by Mgaidi *et al.,* [8] are utilized to validate the computational results for certain cases.

2. Methodology

2.1 Dimpled Rotor Design

The benefits of using a dimple on the rotor's surface have been studied and compared to those of a rotor without a dimple. Three models with different rotor surfaces are proposed, including one with a smooth surface and two with dimples of different sizes. Figure 1 depicts the dimpled rotor design in two variations of width and depth (models B and C), as well as the smooth rotor design (model A). The dimensions of the dimpled surface are determined by taking into account two parameters: (i) the ratio between the width of the dimpled surface (c) and the rotor diameter (d), denoted as (c/d); and (ii) the ratio between the depth of the dimpled surface (k) and the rotor diameter, denoted as (k/d) [13]. The diameter of the rotor is assumed to be fixed, and the size variations c and k, which influence the surface shape of the rotor, are determined in Table 1. The effect of the two variables c and k on the magnitude of the lifting force caused by the air circulating around the rotor surface is examined. On a rotating rotor, the Magnus effect can occur, so that the rotational speed of the rotor has a significant impact on the magnitude of the lifting force on the rotor surface [7].

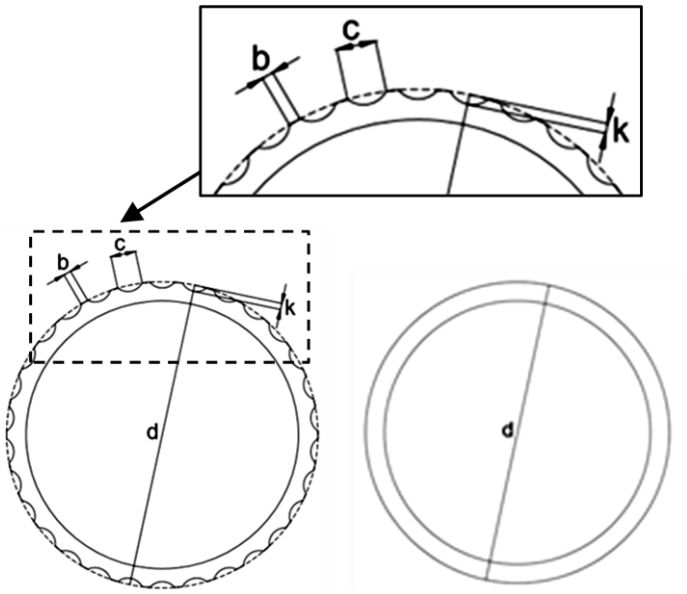

Fig. 1. Rotor cross section (a) with and (b) without dimples

Table 1
Main dimensions of 3 various rotor model

Model	Diameter of rotor (d)	Parametric design	
		c/d	k/d
Model A	3 m	-	-
Model B	3 m	0.08	0.008
Model C	3 m	0.1	0.01

Therefore, the study also examines the effect of the spin ratio (SR), on the value of the generated lift. The SR can be calculated using Eq. (1), where Ω is the rotor's rotational speed (rad/s), and U is the wind speed (m/s).

$$\mathrm{SR} = \frac{\Omega \mathrm{d}}{2\mathrm{U}} \tag{1}$$

SR is calculated according to the scenario shown in Table 2, which has five different variations ranging from 1 to 4, assuming a constant wind speed of 6 m/s, which is the average wind speed at a particular place. When determining which of the five possible SR values to utilize, it is important to keep in mind that the findings of the published Flettner rotor test could be used to validate the computations made by the CFD simulation. The experiment investigation was carried out by Mgaidi *et al.,* [8] in order to quantify the forces acting on a spinning cylinder within the 1m x 1m low speed open loop wind tunnel in the Aerodynamic Laboratory of the Aerospace Engineering Department in the UPM. The experiments were carried out with free stream velocities of 11 m/s, 13 m/s, and 15 m/s using the real model, which consisted of a circular cylinder with a diameter (d) of approximately 0.08 m rotating at an angular velocity of 2010, 2293, 2590, and 2850 revolutions per minute.

Table 2
Variation of Spin Ratio (SR)

Spin Ratio (SR)	Wind speed (m/s)	Rotating speed of rotor (rad/s)
1	6	4
1,5	6	6
2	6	8
3	6	12
4	6	16

2.2 Fitted Flettner Rotor on the Ship

The Maruta Jaya 900 DWT sailing ship is used to evaluate the practicality of the Flettner rotor design, which is chosen from three offered designs with the highest value for generating lift. The placement of the rotor on the ship's deck takes into account the total size of the vessel and the available space on the main deck. The ship's primary dimensions are listed in Table 3, and the rotor is put in the same location as the mast [15]. The rotor's height has been built to be lower than the existing sail's center of gravity. The rotor is intended to have a height of 26 meters above the main deck, with the center of gravity placed 13 meters above the deck. On the main deck, there is a distance of 5d (5 times the outer rotor's diameter) between the two rotors, as shown in Figure 2.

Table 3
Main dimensions of Maruta Jaya sailing ship

Item	Dimension	Unit
Lwl	51.6	m
Lpp	50	m
Breadth (B)	12	m
Height (H)	5	m
Draft (T)	4.7	m
Voyage speed	6	knot
Coefficient Block (Cb)	0.56	
Displacement	1623.5	ton

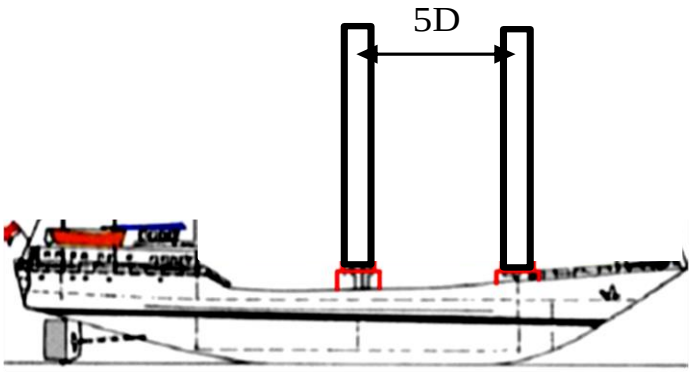

Fig. 2. Fitted Rotor on the main deck of the Maruta Jaya ship

Similar to the forces acting on the sail, the Flettner rotor's thrust can be considered a driving force. Increasing the driving force, FR, which is a force in the forward direction of the ship, is the key to achieving optimal rotor thrust. Eq. (2) shows that the driving forces can be found by multiplying the coefficient of driving force, C_R, by the wind's free-flow dynamic speed and the rotor's surface area, A. And the driving force coefficient can be computed using Eq. (3) and Eq. (4), where C_L and C_D represent the lift and drag coefficients, respectively, and represent the apparent wind angle relative to the ship's forward movement.

$$\mathrm{FR} = 0.5\mathrm{C_R}\rho\mathrm{AU}^2 \quad (2)$$

$$\mathrm{C_R} = \mathrm{C_L}\sin\alpha - \mathrm{C_D}\cos\alpha \quad (3)$$

$$\mathrm{C_L} = \mathrm{L}/0.5\ \rho\mathrm{AU}^2\ ;\ \mathrm{C_D} = \mathrm{D_r}/0.5\ \rho\mathrm{AU}^2 \quad (4)$$

Figure 3 shows the forces that the apparent wind is exerting on the ship's rotor [16]. The CFD simulation is conducted to predict lift force, L, and drag force, D_r, for various wind directions and rotor rotation rates. In actuality, the driving force that propels the ship forward is stronger than the total resistance force, R_T, that the hull and rotors produce. However, the contribution of the Flettner rotor to the forward speed of the ship may be estimated based on the parameters of the spin ratio 1 to 4 and the apparent wind angle 0° to 360°.

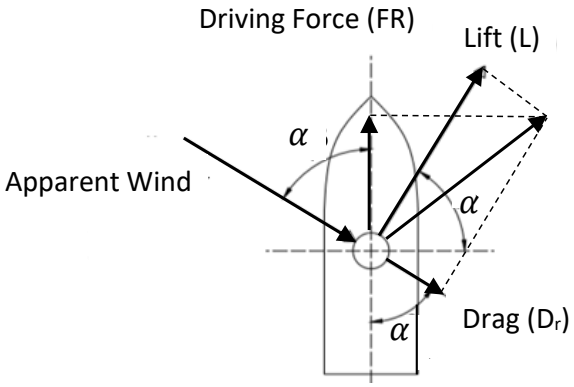

Fig. 3. The forces acting on the ship's rotor

2.3 CFD Setup

Fluent is a well-known CFD tool for solving Reynolds-Averaged Navier-Stokes Equations (RANSE) based problems of fluid interaction with solid objects. The 2-dimensional CFD model is used to examine the dimpled rotor design to generate lift. The general principle of CFD setup follows the

stages of pre-processor, solver configuration, and post-processor. Modeling, establishing boundary conditions, and meshing are the three primary processes of the pre-processor stage. Defining the simulation's boundary area is an important step because it affects the simulation's accuracy and duration. The simulation domain is essentially divided into two domains, namely the rotating domain and the fixed domain, necessitating the use of a dynamic mesh method with an interface technique that combines the two domains. The rotating domain is the region where the mesh is rotated in accordance with the rotor's rotational speed. Thus, it is believed that the simulation results are highly accurate, and the fluid flow around the rotor can be clearly visualized. These two domain sizes correspond to the number of rotors analyzed in the simulation, as shown in Figure 4, which depicts the domain size for one rotor and two rotors, respectively. The inlet boundary line is 5 D (D is the inner diameter of the rotor's boundary) in front of the rotor model, and the outlet boundary is 27.5 D behind the rotor model. The wall boundary lines are 7.5 D from the rotor model's center on both the bottom and top sides. The domain limit for the 2-rotor simulation is essentially identical to that of the 1-rotor simulation, with the exception that the distance between adjacent rotors is 5 D, resulting in inlet and outlet widths of 20 D.

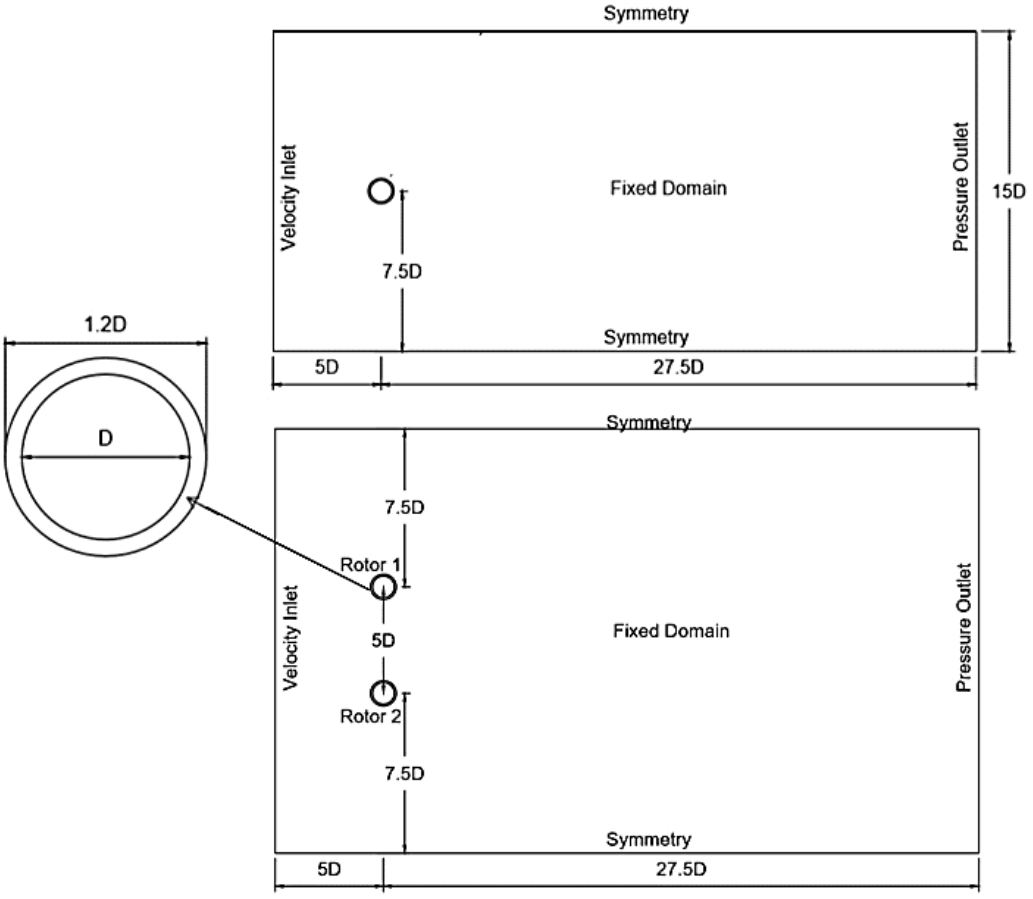

Fig. 4. Domain of one and two rotors model

In all regions with boundary conditions, meshing is done with a hybrid mesh made up of a quadrilateral (structured mesh) in the rotor region and a triangular (unstructured mesh) in the rotating domain and fixed domain regions. In the border region between the rotating domain and the fixed domain, edge sizing is employed to ensure that the meshing size is the same. In the area surrounding the rotor, edge sizing is used, whereas in the rotating domain, face sizing is used, so that the meshing density varies from the rotor area to the fixed domain. In order to capture the boundary

layer flow in the rotor wall region, a structured mesh is utilized. An independent mesh study determines the size and quantity of meshes used in the simulation. The results of which are described in the following section, and the meshing size is shown in Table 4. Figure 5 depicts an overview of the meshing in the 1 and 2-rotor domains, and the region surrounding the rotor surface requires high resolution meshing.

Table 4
Meshing in the domain of simulation

Item	Mesh size	Detail
Rotor	edge sizing	Element size = 0.002 m First layer height = 5 x 10^{-5} m Maximum layers = 20 Growth rate = 1.2
Interface 1 and 2	edge sizing	Element size = 0.02 m
rotate	face sizing	Element size = 0.02 m

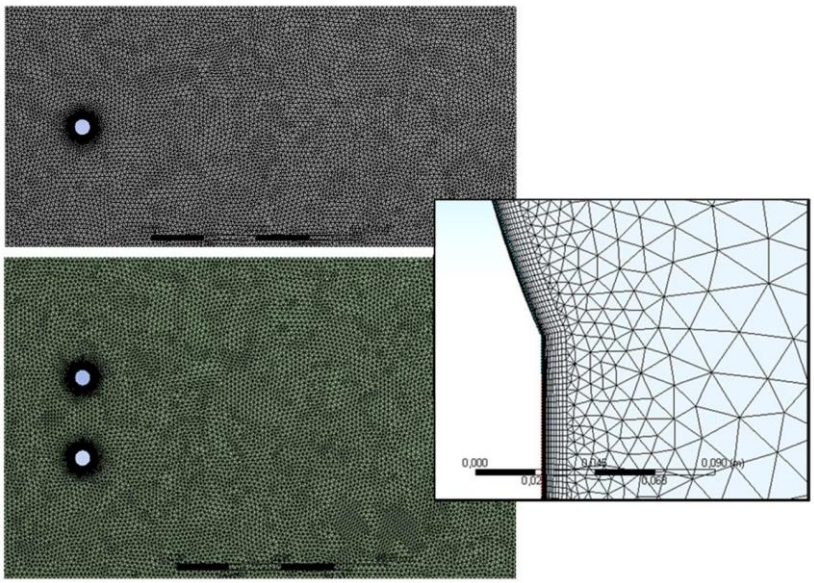

Fig. 5. Meshing of one and two rotors, and detail around rotors

In the inlet region, the fluid flow velocity is 6 m/s with a turbulent intensity of 5 percent and a turbulent viscosity ratio of 10. The default fluid flow setting at the outlet is the sum of the backflow pressures brought about by turbulent flow in the interim. The wall is immobile, there is no slippage, and the standard roughness model has a constant value of 0.5. Setting mesh interfaces is a function that joins two merged interfaces together so that there is no space between them. A dynamic mesh setup is required to define the observed object's motion within the simulation domain. The code uses the UDF (user-defined functions) facility to program the rotation of the rotor, which is based on the spin ratio value. By selecting mesh methods: smoothing and layering, the dynamic mesh task page is accessed. The simulation's solution method consists of pressure-velocity coupling with spatial discretization, specifically a Gree-gauss node based on gradient, presto! of pressure, quick of momentum, turbulent kinetic energy, and dissipation rate. The solution initialization method utilizes hybrid and run-calculation with three settings, such as time step size, number of time steps, and maximum number of iterations. Adjusting the maximum iterations and time steps results in convergence. Post-processing is the processing and visualization of simulation results in views such as pressure contours, velocity contours, streamlines, and vector plots, among others, based on the

requirements of analysis. The visualization is useful for observing the flow phenomena that occur around the rotor.

2.4 Turbulence Flow Model

The CFD flow solver utilized the incompressible unsteady Reynolds-averaged Navier Stokes equations (RANSE), while the k–ω STT model was utilized to solve the turbulence problem. Transport equations are spatially discretized by means of the finite volume method. The velocity field is computed using momentum conservation equations, whereas the pressure field is derived by transforming the continuity equation into a pressure equation [17]. Additional transport equations are discretized and solved according to the same principles as the Euler equation in turbulent flows. In Eq. (5) and Eq. (6), which represent the continuity and Euler equations in terms of tensors, u is the flow velocity, ρ is fluid density, μ is dynamic viscous, F is an external force, and *t* is time. The k-ω SST model has been shown to be numerically stable, especially in the viscous sublayer close to the wall [18]. Due to the high values of in the wall regions, this k-ω SST model does not require explicit wall damping functions. In the numerical wall boundary conditions, the distance between the wall and the first point beyond the wall must be specified. The transport model equations for the k and ω scalar turbulence scales are described in Eq. (7) and Eq. (8), respectively.

$$\frac{\partial \rho}{\partial t} + u_i \frac{\partial \rho}{\partial x_i} + \rho \frac{\partial u_i}{\partial x_i} = 0 \tag{5}$$

$$\rho\left(\frac{\partial u_i}{\partial t} + u_i \frac{\partial u_i}{\partial x_i}\right) = -\frac{\partial p}{\partial x_i} + \mu \frac{\partial^2 u_i}{\partial x_i^2} + F_i \tag{6}$$

$$\frac{\partial(\rho k)}{\partial t} + \frac{\partial\left(\rho u_j k\right)}{\partial x_j} = P - \beta^* \rho \omega k + \frac{\partial}{\partial x_j}\left[\left(\mu + \sigma_k \frac{\rho k}{\omega}\right)\frac{\partial k}{\partial x_j}\right] \tag{7}$$

$$\frac{\partial(\rho \omega)}{\partial t} + \frac{\partial\left(\rho u_j \omega\right)}{\partial x_j} = \frac{\alpha \omega}{k} P - \beta \rho \omega^2 + \frac{\partial}{\partial x_j}\left[\left(\mu + \sigma_\omega \frac{\rho k}{\omega}\right)\frac{\partial \omega}{\partial x_j}\right] \tag{8}$$

Where α = 0.52, β = 0.075, β^* = 0.09, $\sigma_k = \sigma_\omega$ = 0.5 [18, 19].

3. Results and Discussion

3.1 Mesh Independence Study and Validation

The mesh independence study aims to determine the optimal number and size of meshes in terms of simulation time and accuracy of results. If the simulation results do not vary by more than one percent as the number of elements increases, the number of meshes is deemed optimal. Observing simulation results as parameters, such as the lift coefficient (C_L) and the drag coefficient (C_D) acting on the rotor surface, simulation is done on the one-rotor and two-rotor models with an incoming wind angle of 90^o and a speed of 6 m/s. As shown in Figure 6 of a one-rotor model B, the addition of elements from 157,845 to 250,659 resulted in 0.68% and 0.19% differences in C_L and C_D, respectively. Since differences are less than 1%, the ideal number of meshes for a single rotor is determined to be 157,845. The simulation results for the two-rotor model show that in the case of adding elements from 309,604 to 620,301, the differences in C_L in rotors 1 and 2 are 0.65% and 0.43%, respectively, while the differences in C_D are 0.48% and 0.31%, respectively. For a two-rotor case, the optimal number of meshes is 309,604. (See Figure 6).

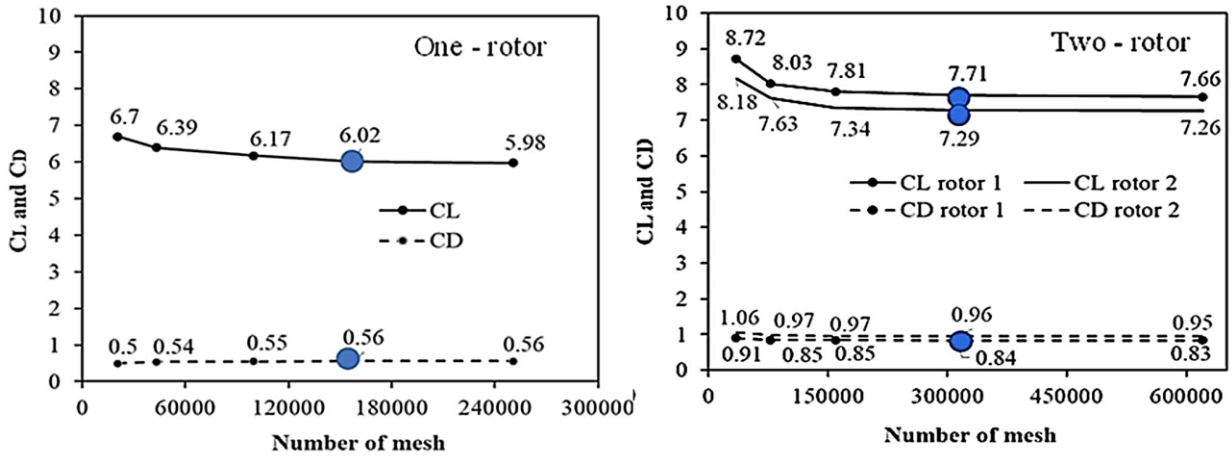

Fig. 6. Independence study of mash for one rotor and two rotors

The CFD settings have a direct impact on the results of the computational fluid dynamics simulations. As a result, the results of the CFD simulation are verified by comparing them to the results of the wind tunnel tests done on the rotor model, which are described in [8]. The CFD setup has to be compliant with the test operating conditions, which include the diameter of the rotor model being 8 cm, the wind speed being 13 m/s, and the environmental setup, which includes an atmospheric pressure of 1.01 x 10^5 N/m^2, a temperature of 306.15 K, an air density of 1.154 Kg/m^3, and an air viscosity of 1.87 x 10^5 Kg/m.sec. Figure 7 shows a difference of between 1% and 4% between the results of CFD and experiments done to find the coefficient of lift. The graph demonstrates that the lift coefficient for a rotor model that does not include dimples grows in a linear fashion in relation to the number of spins that occur per minute. Given that the CFD setup is within the margin tolerance criterion of less than 5%, it is possible to regard it as being quite genuine.

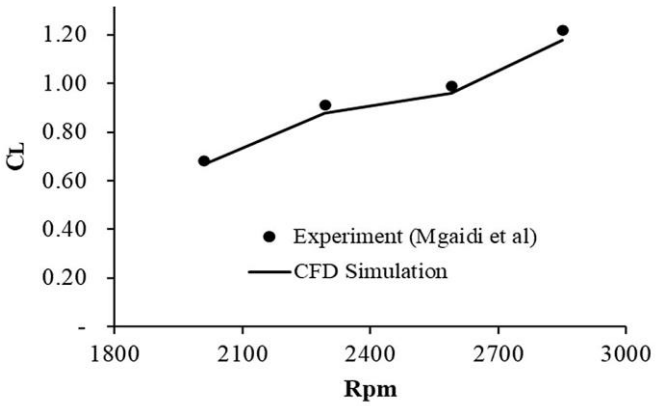

Fig. 7. Comparison of the model test and CFD results

3.2 Simulation Results of One Rotor

Figures 8 and 9 show the simulation results in the form of lift and drag coefficients for the spinning rotor models A, B, and C with five different spin ratios (SR) ranging from 1 to 4. The figures are an illustration of the link between the spin ratio and the lift and drag coefficients in each model. Figures 10 and 11 illustrate the fact that the contours of the pressure distribution are unique for models A, and C for the scenarios in which SR equals 1 and 4, respectively. Because of the difference in pressure that exists between the upper and lower surface areas of the rotor, there is an upward

force that is exerted from regions with high pressure to regions with low pressure. This force is exerted from regions where the pressure is higher to regions where the pressure is lower [20].

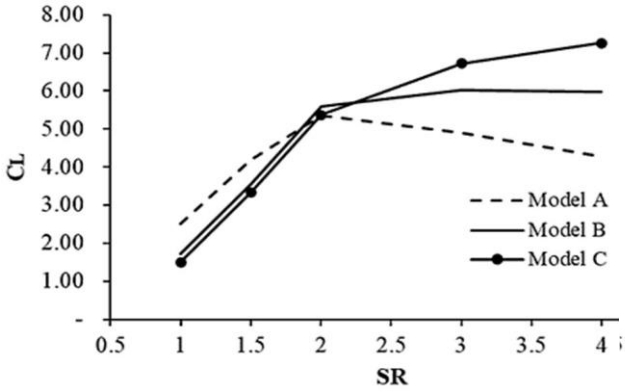

Fig. 8. Comparison of C_L for Model A, B, and C

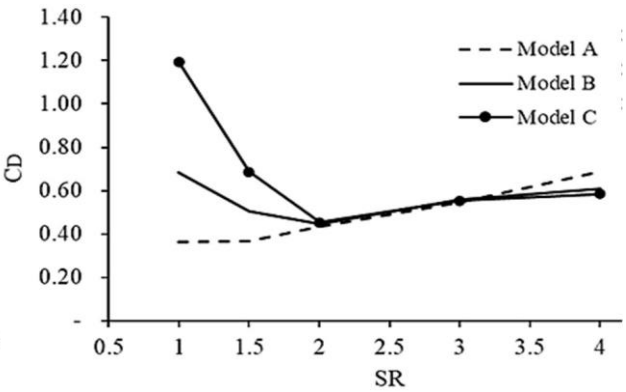

Fig. 9. Comparison of C_D for Model A, B, and C

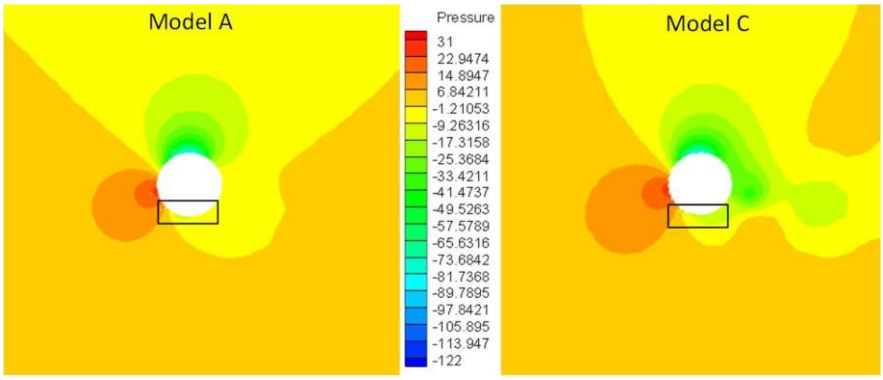

Fig. 10. Contour of pressure at SR = 1

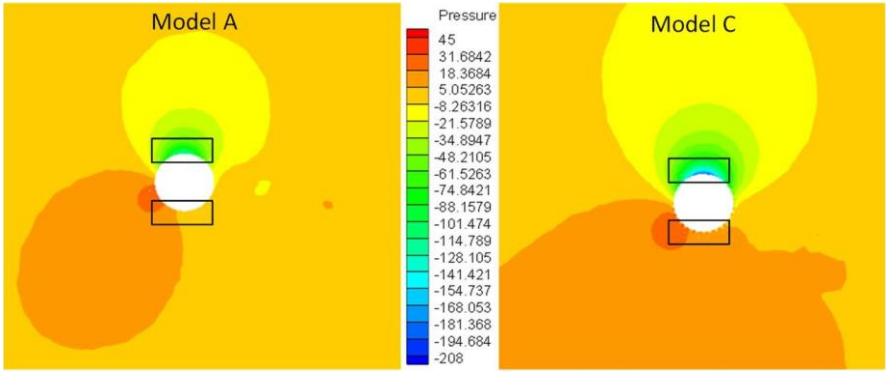

Fig. 11. Contour of pressure at SR = 4

More specifically, the curves in Figures 8 and 9 show that when the SR is between 1 and 2, C_L tends to grow, but C_D tends to decrease. After SR = 2, Model A faces a loss of thrust because the lift coefficient decreases when SR is equal to 3 or 4. Model B exhibits a distinct behaviour by coming to a complete stop at SR 3. Stalling, on the other hand, does not occur in Model C until SR equals 4, and possibly even later. The coefficient of drag for Models B and C went from SR equal to 1 to 2 with a negative value, but it goes back up to around the same level after SR greater than 2. This is a different occurrence from the one that is found in Model A, in which the drag coefficient rose from SR equal to 1 up to 4. The use of the dimpled surface on the rotor provides an advantage by increasing the lift coefficient and lowering the drag coefficient, provided that SR is less than 2. At SR = 3, the lift

coefficient of a surface with dimples is 37.5% greater than the lift coefficient of a surface without dimples, and at SR 4, it is 69.6% higher.

The highest reduction in the drag coefficient that may occur is 14.8% when SR is equal to 4. When SR is equal to 1 and 1.5, the rotor that does not have a dimpled surface (Model A) provides a lift coefficient that is up to 66.9% and 25.9% bigger than the dimpled surfaces that are found on Models B and C, respectively. The lift coefficient of Model C (c/d = 0.1, k/d = 0.01) is greater than that of Model B (c/d = 0.08, k/d = 0.008), which is 11.6% and 21.4% at SR = 3 and 4, respectively. The fact that the size of the dimpled surface, as measured by c/d and k/d, respectively, influences the lift and drag coefficients serves as evidence for this. When SR is equal to 3 and 4, Model C has a drag coefficient that is 1.5% and 3.9%, respectively, lower than that of Model B. Given this, Model C is the best option when SR is greater than 2, and Model A is the best option when SR is less than 2, given that both models offer the maximum lift and the lowest drag coefficients. As a result, Model C is the best option when SR is greater than 2, and Model A is the best option when SR is less than 2. Figures 12 illustrate the distribution pressure for the top and bottom regions of Models A and C, respectively. When SR equals 4, the difference in pressure between the bottom and upper portions of Model C is noticeably bigger than that of Model A. On the other hand, when the SR is set to 1, Model A has a pressure that is marginally greater than Model C.

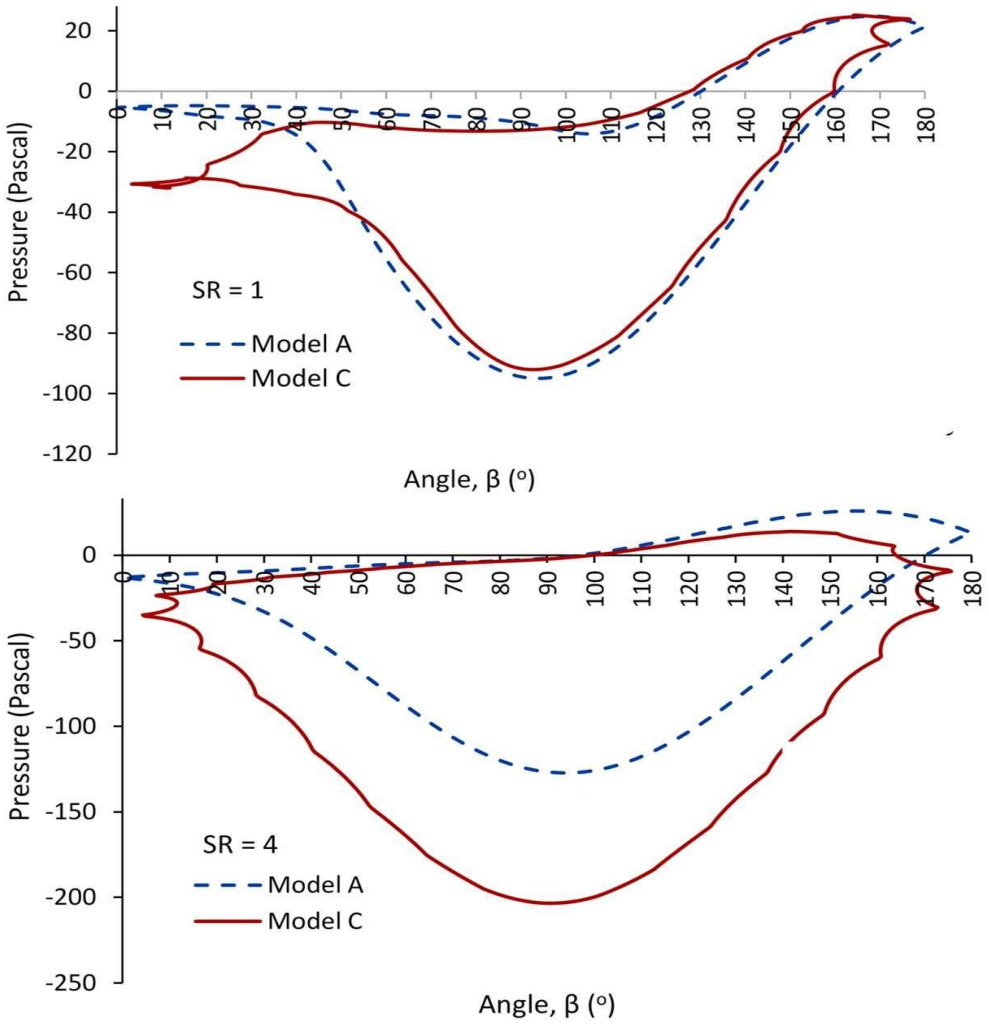

Fig. 12. Pressure distribution of model A and C, at SR = 1 and SR = 4

3.3 Simulation Results of Two Rotors

Figure 13 depicts the lift and drag coefficients found for the two rotors and the contour of pressure depicted in Figure 14. The data analysis led to the conclusion that Model C with a spin ratio of 4 should be utilized. In the simulation of two rotors, fluid interference occurs between Rotor 1 and Rotor 2, the intensity of which varies depending on the wind direction [21]. Each rotor's performance is tested at 0°, 30°, 60°, and 90°, which correspond to the four different wind angles. According to the C_L comparison graph, the interference between Rotor 1 and Rotor 2 occurs in all possible wind direction configurations. As a result, one of the rotors has a greater lift coefficient than the others. The greatest difference in lift coefficient between Rotor 1 and Rotor 2 occurs at an incidence angle of 0°, which is where the interference is the most severe. When the wind is blowing in at a 30° or 90° angle, interference tends to diminish. One possible explanation for the variation in C_D between the two rotors is that Rotor 1 and Rotor 2 encounter an interference effect on their respective drag coefficients. The fact that the difference in drag between Rotor 1 and Rotor 2 is decreasing illustrates how the drag coefficient tends to decrease as the wind angle increases from 0° to 90°.

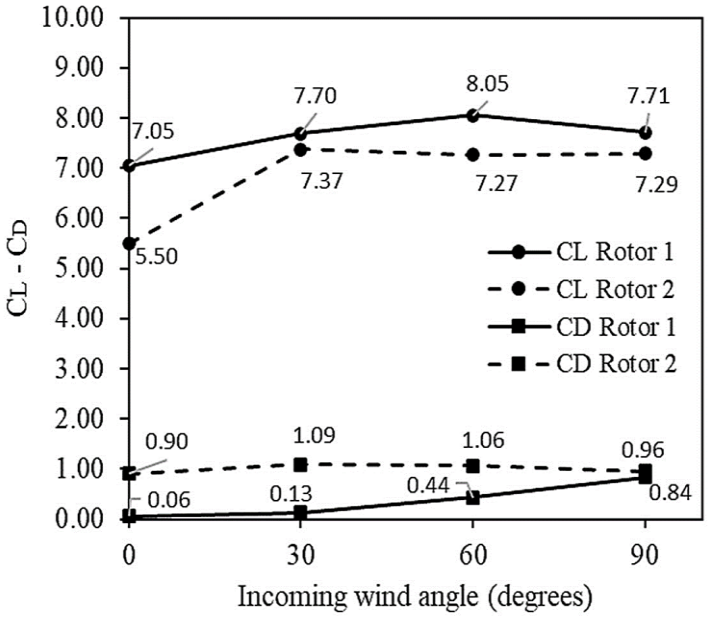

Fig. 13. C_L and C_D due to incoming wing angle at Rotor 1 and Rotor 2

3.4 Rotors Mounting on Ship

The installation of the rotor on the ship raises the ship's LWT, which increases the ship's draft as well as its resistance. The estimated total weight of the sails and mast of the Maruta Jaya 900 DWT is 44 tons, while the weight of the two rotors is calculated to be 51 tons, resulting in an increase of 7.55 tons in the ship's total weight or an increase in displacement to 1,631 tons. The change in draft height, which is increased by roughly 2 cm, and the consequent change in ship resistance are quite minor and can be described as insignificant. However, the placement of the rotor on the ship's deck also influences the ship's wind resistance. The rotor resistance comes from a CFD simulation, as shown in Table 5, which also shows the hull resistance of the Maruta Jaya 900 DWT based on the results of towing tests done at HVSA West Germany (test report sheet dated May 6, 1983: test No. 83-144/145) [15]. The sum of the rotor and hull resistances, which the thrust must overcome in order

for the ship to move forward at a certain speed, is the total resistance of the ship. Using Eq. (2) and Eq. (3), the driving force on two rotors of Model C with a spin ratio of 4 is calculated, yielding the maximum value in Table 5.

Table 5
Resistance, driving force and trust of the Maruta Jaya 900 DWT with two rotors

Speed (knots)	Resistance (kN)			Driving Force (FR) (kN)	Thrust (FR-R_T) (kN)
	Hull (HVSA, 1983)	Rotor	Total (R_T)		
4	5.2	0.18	5.38	24.3	18.92
6	11.49	0.41	11.90	24.3	12.40
7.1	15.93	0.58	16.51	24.3	7.79
8.1	20.88	0.75	21.63	24.3	2.67
9.1	27.93	0.94	28.87	24.3	-4.57
10.1	38.77	1.16	39.93	24.3	-15.63

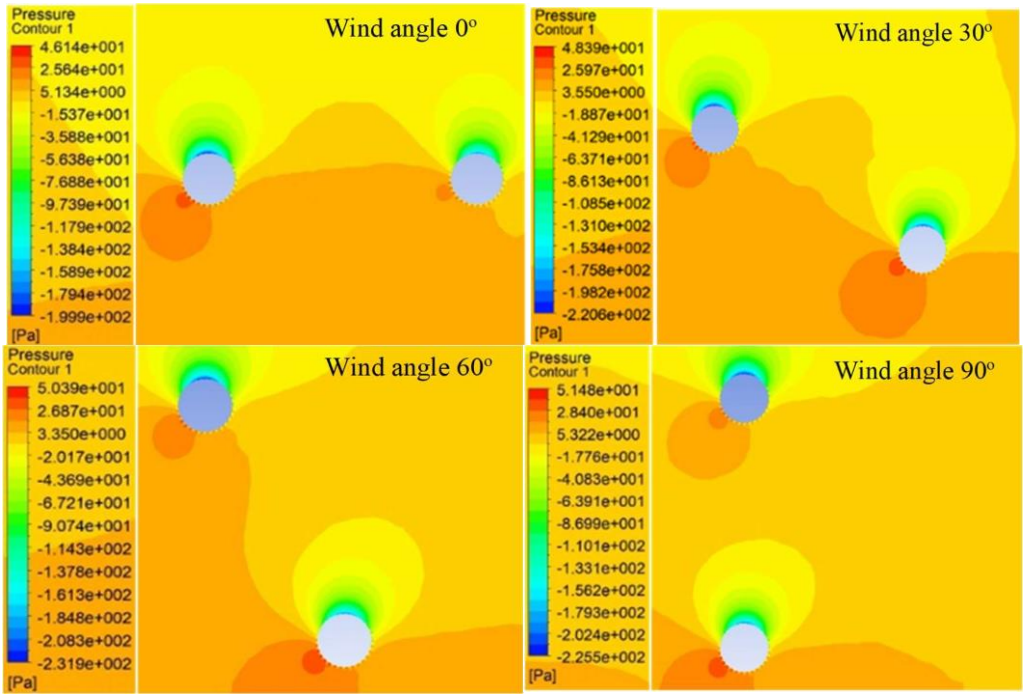

Fig. 14. Contour of pressure at Rotor 1 and Rotor 2

In the case of two rotors of model C with SR = 4, as shown in Fig. 15(a), all calculations of FR are done using Eq. (2). These angles are 0°, 30°, 60°, 90°, 120°, 150°, 180°, 210°, 240°, 270°, 300°, and 330°. The maximum driving force is about 24.3 kN when the incidence of the wind in the direction of the ship's speed is 90° or 270°, and the minimum is about 15.5 kN at 0° or 180° of the incoming wind angles. It is possible to compute the contribution of the thrust to the ship's speed by subtracting the driving force, FR, from the total drag, RT; see Table 5. If FR exceeds RT, the ship is presumed to be sailing at a particular speed. The rotor cannot propel the ship forward while FR is less than or equal to RT. The ship can move forward with a maximum speed of about 8.1 knots. However, the ship's speed can be obtained using Eq. (2), where the ship's thrust equals the difference between FR and RT. Figure 15(b) depicts the driving force and ship's speed in polar coordinates with respect to a 6 m/s wind from 12 various arrival directions.

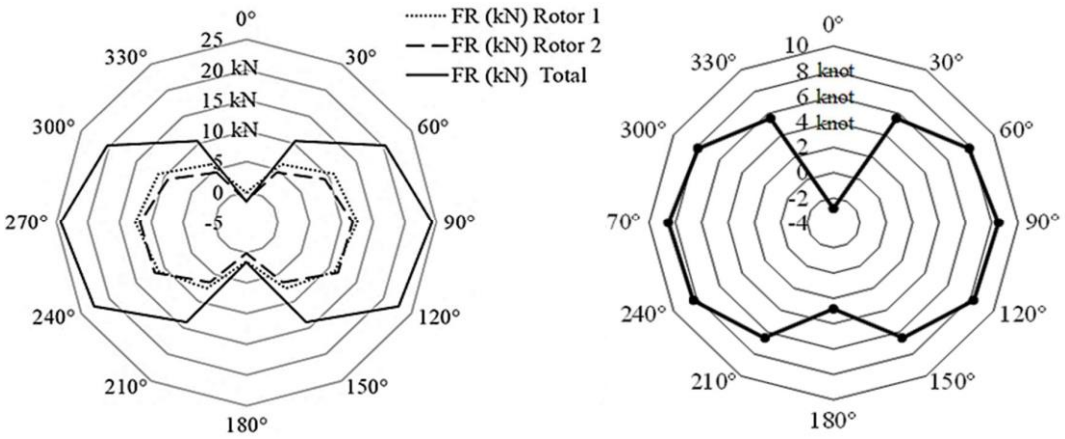

Fig. 15. (a) Driving Force and (b) Ship's speed due to the angle of apparent wind

4. Conclusions

The CFD code is utilized to model the air flow around the Flettner rotor surface at the different spin ratios (SR), which include 1, 1.5, 2, 3, and 4. Using the Reynolds Average Navier-Stokes (RANS) equation and the k-ω model for turbulent flow, the lift and drag coefficients of three rotor designs are determined: a smooth surface model (Model A) and two dimple surface models (Models B and C) with various dimple sizes. The validity of the CFD setup is confirmed by comparing the CFD findings to experimental data acquired in the wind tunnel and concluding that the maximum error is approximately 4%. The simulation findings indicate that adding a dimpled surface to the rotor boosts lift force by up to 69.6% and decreases drag force by 14.76%. The two rotors mounted on the deck of the Maruta Jaya 900 DWT are capable of creating the greatest thrust, giving the ship a speed of 8.5 knots at a spin ratio of 4, while the wind acts at angles of 90° and 270° relative to its speed.

Acknowledgement

The authors are grateful to DRPM Institut Teknologi Sepuluh Nopember (ITS) Surabaya for providing a financial support under the scheme of upgrading TA.

References

[1] Yoshimura, Yasuo. "A prospect of sail-assisted fishing boats." *Fisheries science* 68, no. sup2 (2002): 1815-1818. https://doi.org/10.2331/fishsci.68.sup2_1815

[2] Schmidt, A. Enercon E. "Ship 1 A Wind-Hybrid Commecial Cargo Ship." In *Proceedings of the 4th Conference on Ship Efficiency*, pp. 23-24. 2013.

[3] Sulisetyono, Aries. "The evaluation of a rigid sail of ship using wind tunnel test." *Applied Mechanics and Materials* 493 (2014): 287-293. https://doi.org/10.4028/www.scientific.net/AMM.493.287

[4] Bergeson, Lloyd, and C. Kent Greenwald. "Sail assist developments 1979–1985." *Journal of wind engineering and industrial aerodynamics* 19, no. 1-3 (1985): 45-114. https://doi.org/10.1016/0167-6105(85)90056-X

[5] Prandtl, Ludwig. "The Magnus effect and wind-powered ships." Naturwissenschaften, vol. 13, (1925): 1787–1806.

[6] Seybold, G. S. "A sailing ship without sails: new wonder of the seas." *Popular Science Monthly* 106, no. 2 (1925): 35-37.

[7] De Marco, Agostino, Simone Mancini, Claudio Pensa, Giuseppe Calise, and Fabio De Luca. "Flettner rotor concept for marine applications: A systematic study." *International Journal of Rotating Machinery* 2016 (2016). https://doi.org/10.1155/2016/3458750

[8] Mgaidi, A. M., Azmin Shakrine Mohd Rafie, Kamarul Arifin Ahmad, Rizal Zahari, Mohd Faisal Abdul Hamid, and Omar Faruqi Marzuki. "Numerical and experimental analysis of the flow around a rotating circular cylinder at subcritical regime of Reynolds number using K-E and K-Ω-SST turbulent models." ARPN Journal of Engineering and Applied Sciences, vol. 13, no. 3, (2018): 954-960.

[9] Li, Boyang, Rui Zhang, Yajing Li, Baoshou Zhang, and Chao Guo. "Study of a new type of Flettner rotor in merchant ships." *Polish Maritime Research* (2021). https://doi.org/10.2478/pomr-2021-0003
[10] Zhou, Bo, Xikun Wang, Wei Guo, Wie Min Gho, and Soon Keat Tan. "Control of flow past a dimpled circular cylinder." *Experimental Thermal and Fluid Science* 69 (2015): 19-26. https://doi.org/10.1016/j.expthermflusci.2015.07.020
[11] Bearman, P. W., and J. K. Harvey. "Control of circular cylinder flow by the use of dimples." *AIAA journal* 31, no. 10 (1993): 1753-1756. https://doi.org/10.2514/3.11844
[12] Butt, Usman, Lothar Jehring, and Christoph Egbers. "Mechanism of drag reduction for circular cylinders with patterned surface." *International journal of heat and fluid flow* 45 (2014): 128-134. https://doi.org/10.1016/j.ijheatfluidflow.2013.10.008
[13] Yahaya, Wan Mohamad Aiman Wan, Syahrullail Samion, Fazila Mohd Zawawi, Mohd Nor Musa, and Muhammad Naim Aiman Najurudeen. "The evaluation of drag and lift force of groove cylinder in wind tunnel." *Journal of Advanced Research in Fluid Mechanics and Thermal Sciences* 68, no. 2 (2020): 41-50. https://doi.org/10.37934/arfmts.68.2.4150
[14] Aoki, Katsumi, Koji Muto, and Hiroo Okanaga. "Aerodynamic characteristics and flow pattern of a golf ball with rotation." *Procedia Engineering* 2, no. 2 (2010): 2431-2436. https://doi.org/10.1016/j.proeng.2010.04.011
[15] Tantin, Titik Rus. "Analisa system propulsi berpenggerak motor listrik pada kapal klas Maruta Jaya 900 DWT." PhD diss., Institut Teknologi Sepuluh Nopember, 2005.
[16] Marchaj, C. A. (1964) Sailing Theory and Practice, Dodd Mead & Company, New York, United States.
[17] Versteeg, Henk Kaarle, and Weeratunge Malalasekera. An introduction to computational fluid dynamics: the finite volume method. Pearson education, 2007.
[18] Wilcox, D. C. (1998) Turbulence Modeling for CFD. 2nd edition, DCW Industries, Inc., La Canada CA.
[19] Aliffrananda, M. H., Aries Sulisetyono, Yuda Apri Hermawan, and Achmad Zubaydi. "Numerical analysis of floatplane porpoising instability at calm water during take-off." *International Journal Technology* 13, no. 1 (2022): 190-201. https://doi.org/10.14716/ijtech.v13i1.4903
[20] Sulisetyono, Aries, And Rinaldi E. Wardhana. "The Resistance Evaluation Of The Autonomous Underwater Vehicle (Auv) Using The Low Speed Wind Tunnel Test." *Journal Of Engineering Science And Technology* 17, No. 6 (2022): 4355-4366.
[21] Anwar, Shoaib, Md Ibrahim Khalil, and Sumon Saha. "Finite Element Analysis on Turbulent Flow Over Two Side-by-Side Rotating Cylinders." In *Proceedings of the 11th International Conference on Computer Modeling and Simulation*, pp. 107-111. 2019. https://doi.org/10.1145/3307363.3307380